

# Two-phase MPM modelling of debris flow impact against dual rigid barriers

CHARLES WANG WAI NG\*, ZHENYANG JIA†, SUNIL POUDYAL‡, AASTHA BHATTA§ and HAIMING LIU||

Multiple barriers are usually installed to effectively mitigate large-volume debris flows. Existing multiple-barrier design recommendations ignore the effects of solid–fluid interaction and may cause uncertainties in estimating the flow impact force on subsequent barriers. In this study, a fully coupled, two-layer, two-phase material point method with an incompressible fluid phase is implemented and validated using the experimental results of dry sand, water and sand–water mixture flows impacting on rigid barriers. Numerical parametric study is carried out using the validated model to investigate the effects of Froude number ( $Fr$ ) and barrier spacing on second barrier impact force. A debris flow volume of  $500 \text{ m}^3$  is modelled, with the  $Fr$  ranging from 2 to 6; these are values relevant to the gentle and steep terrains in Hong Kong. Simulation results show the importance of changes in fluidisation ratio, which is the ratio of basal pore fluid pressure and total stress. The debris flow, after impacting the first barrier, overflows and lands on the slope between the two barriers. The fluidisation ratio of debris flow after landing increases by up to 30%, leading to an increase of impact velocity at the second barrier by up to 80%. Consequently, the impact force of debris flows on the second barrier is underestimated by up to 50% compared with existing design guidelines. This implies that neglecting the fluidisation ratio may lead to non-conservative design of multiple barriers.

**KEYWORDS:** landing; landslides; multiple barriers; numerical modelling; two-phase

## INTRODUCTION

Multiple barriers are designed to blend into the topography, to progressively deposit and retain large volumes of debris flow along the flow path and ultimately to reduce the barrier size (Wong, 2009; Kwan *et al.*, 2015; Ng *et al.*, 2018, 2021). Existing design guidelines (VanDine, 1996; CGS, 2004) for multiple barriers consider only the total retention volume and neglect the dynamic flow–barrier interaction. This may be reasonable for gentle terrain where the debris flows have lower Froude conditions. However, for steep terrain, neglecting the interaction may lead to non-conservative design for subsequent barriers due to higher Froude conditions of overflow.

To estimate the peak impact force, existing design guidelines for a debris-resisting barrier mainly consider two force components: the hydrodynamic (Kwan, 2012; ASI, 2013; Cui *et al.*, 2015) and the hydrostatic forces

(NILIM, 2016; Armanini *et al.*, 2020), given as follows

$$F = \alpha \rho v^2 h + \frac{1}{2} k h^2 \rho \|g\| \quad (1)$$

where  $\alpha$  and  $k$  are dynamic and static impact coefficients, respectively;  $\rho$  is the density of debris flows;  $v$  and  $h$  are the flow velocity and flow depth at the barrier location, respectively; and  $\|g\|$  is the magnitude of gravitational acceleration. Ng *et al.* (2020a) recommend the dynamic and static impact coefficients,  $\alpha$  and  $k$ , as unity for designing the second barrier of dual rigid barriers. Flow velocity and flow depth are the governing flow variables required to estimate the hydrodynamic and hydrostatic forces on a barrier. These two variables can be reasonably estimated for a single barrier impact using depth-averaged debris mobility analysis (McDougall & Hungr, 2004). The maximum flow depth  $h_{\text{flow}}$  and velocity  $v_{\text{flow}}$  at a barrier location in free-flow conditions can conservatively estimate the impact force on a barrier (Kwan, 2012). However, the evolution of flow depth and flow velocity during barrier interaction with overflow and landing in multiple barriers cannot be predicted since the depth-averaged framework neglects momentum transfer normal to the slope.

To tackle the above-mentioned drawback of a depth-averaged framework, Kwan *et al.* (2015) proposed a point-mass method to estimate the overflow and landing kinematics combined with debris mobility analysis. Fig. 1 shows a schematic representation of the method. The flow depth after landing  $h_i$  is assumed not to exceed  $h_{\text{flow}}$  (Fig. 1(a)) obtained from debris mobility analysis, ignoring the changing depth during launch ( $h_{\text{launch}}$ ). The velocity just before landing can be calculated by assuming energy conservation of a point mass and is given as follows

$$v_r = \sqrt{v_{\text{launch}}^2 + 2\|g\| \left[ \frac{H_B}{\cos \theta} + (x_i - H_B \tan \theta) \sin \theta \right]} \quad (2)$$

Manuscript received 21 June 2022; revised manuscript accepted 25 January 2023.

Discussion on this paper is welcomed by the editor.

\* Department of Civil and Environmental Engineering, The Hong Kong University of Science and Technology, Hong Kong SAR, P. R. China (Orcid:0000-0001-6693-3151).

† Department of Civil and Environmental Engineering, The Hong Kong University of Science and Technology, Hong Kong SAR, P. R. China (Orcid:0000-0002-3023-1024).

‡ Department of Civil and Environmental Engineering, The Hong Kong University of Science and Technology, Hong Kong SAR, P. R. China (Orcid:0000-0002-3259-745X).

§ Department of Civil and Environmental Engineering, The Hong Kong University of Science and Technology, Hong Kong SAR, P. R. China (Orcid:0000-0003-4879-7269).

|| Department of Civil and Environmental Engineering, The Hong Kong University of Science and Technology, Hong Kong SAR, P. R. China (Orcid:0000-0003-1235-6058).

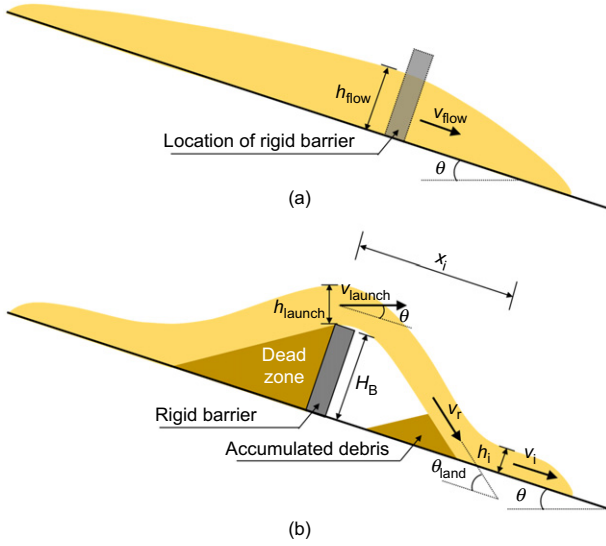


**Fig. 1. Schematic diagram of point mass method on prediction of trajectory distance  $x_i$  and landing velocity  $v_i$ : (a) free-flow condition; (b) interaction with single barrier**

where  $v_{\text{launch}}$  is the launch velocity at the crest of the first barrier;  $H_B$  is the barrier height;  $\theta$  is the inclination of the slope; and  $x_i$  is the landing distance. The landing distance is calculated based on point mass approximation of the flow front (Ng *et al.*, 2018, 2020a, 2021), assuming  $v_{\text{launch}}$  is perpendicular to gravity, and is given as follows

$$x_i = \frac{v_{\text{launch}}^2}{\|g\|\cos\theta} \left( \tan\theta + \sqrt{\tan^2\theta + \frac{2\|g\|H_B}{v_{\text{launch}}^2 \cos\theta}} \right) + H_B \tan\theta \quad (3)$$

During landing, the impact of flow on the bed is assumed to be fully plastic, and thus the flow velocity normal to the slope becomes zero after landing. The flow velocity after landing is expressed as the slope-parallel component of  $v_r$ , considering a certain amount of energy dissipation and is given as follows

$$v_i = R v_r \cos\theta_{\text{land}} \quad (4)$$

where  $\theta_{\text{land}}$  is the angle between  $v_r$  and the bed.  $R$  is a velocity correction factor to consider energy dissipation caused by the stiffness of the soil bed and the interaction of overflowing debris with landed material. Ng *et al.* (2020a) proposed  $R = 1.0$  as an upper-bound value, assuming no energy dissipation along the slope-parallel direction during landing. The flow depth and velocity are then implemented in a debris mobility analysis (Hung, 1995; Kwan & Sun, 2006) to compute the flow depth and velocity impacting on a subsequent barrier.

In the debris mobility analysis, the debris flow is assumed to be an equivalent fluid, where an equivalent bed friction angle is used to implicitly consider the decrease of effective stress caused by basal pore fluid pressure. The equivalent fluid method assumes the change of pore fluid pressure is not significant. However, the rapid undrained loading during impact of debris flow against barriers and the subsequent overflow and landing processes may lead to an increase in pore fluid pressure (Kwan *et al.*, 2015; Song *et al.*, 2022). This increase of pore fluid pressure cannot be captured by the equivalent fluid method. As such, the impact velocity and impact force of two-phase debris flow on a downstream barrier may be underestimated by the equivalent fluid method. Apparently, understanding the two-phase flow dynamics during and after landing is essential to design the subsequent barriers in multiple-barrier systems.

In this study, the impact dynamics of two-phase debris flow against dual rigid barriers are investigated using a fully coupled two-phase material point method (MPM). Physical flume tests are used to calibrate the two-phase MPM model. Numerical parametric study is carried out to investigate the effects of Froude number and barrier spacing on the interaction between two-phase debris flows and dual rigid barriers. A comparison of modelling debris flow using equivalent fluid model and two-phase model is carried out to highlight the importance of two-phase simulation.

## TWO-PHASE MATERIAL POINT METHOD

The MPM serves as an efficient meshless method to model large-deformation problems (Lian *et al.*, 2012; Mast *et al.*, 2015; Li *et al.*, 2021) with a balance between spatial resolution and computational time (Soga *et al.*, 2016). In this study, a fully coupled two-phase MPM based on a two-layer formulation for solid and fluid phases is used in modelling debris flow impact against dual rigid barriers. Two sets of material points are used to separately simulate the solid and fluid phases. The flow behaviour of the solid phase is modelled using the shear rate-dependent non-associated Drucker–Prager yield criterion, whereas the fluid phase is modelled as an incompressible fluid with Newtonian rheology. The solid and fluid phases interact through inter-phase forces, including the force induced by the pore fluid pressure gradient and the force due to relative motion between the two phases.

To emphasise the importance of the two-phase model, the flow depth, velocity and impact force on barriers computed from an equivalent fluid model (Gao *et al.*, 2017; Kwan *et al.*, 2019; Zhao *et al.*, 2020) are compared with that of the two-phase model. The equivalent fluid model is achieved by only considering the solid phase material points of the two-phase model with equivalent internal and bed friction angles.

### Governing equations

The motions of the two-phase material points are governed by the momentum equations expressed as follows (Bandara & Soga, 2015; Baumgarten & Kamrin, 2019)

$$\bar{\rho}_s \frac{D\mathbf{v}_s}{Dt} = \bar{\rho}_s \mathbf{g} + \nabla \cdot \boldsymbol{\sigma}' - \mathbf{f}_d - \phi \nabla p_f \quad (5)$$

$$\bar{\rho}_f \frac{D\mathbf{v}_f}{Dt} = \bar{\rho}_f \mathbf{g} + \nabla \cdot \mathbf{T}_f + \mathbf{f}_d - (1 - \phi) \nabla p_f \quad (6)$$

where subscripts 's' and 'f' represent solid and fluid phases, respectively;  $\bar{\rho}$  is the effective density;  $D(\cdot)/Dt$  denotes material derivatives;  $\mathbf{v}$  is the velocity vector;  $\mathbf{g}$  is gravitational acceleration;  $\nabla \cdot \boldsymbol{\sigma}'$  is the divergence of effective stress of the solid phase;  $\nabla \cdot \mathbf{T}_f$  is the divergence of the viscous shear response of the fluid phase;  $\mathbf{f}_d$  is the inter-phase body force;  $\phi$  is the solid volume fraction; and  $\nabla p_f$  is the gradient of the pore fluid pressure.  $\bar{\rho}_s$  and  $\bar{\rho}_f$  are defined as follows

$$\bar{\rho}_s = \phi \rho_s \quad (7)$$

$$\bar{\rho}_f = (1 - \phi) \rho_f \quad (8)$$

where  $\rho_s$  is the solid density and  $\rho_f$  is the fluid density.

### Constitutive models and model parameters

#### Fluid phase: incompressible fluid with Newtonian rheology.

The fluid phase in two-phase MPM is generally regarded as a weakly compressible phase in dynamic problems to compute the pore fluid pressure,  $p_f$  (Monaghan, 1994;

Morris *et al.*, 1997; Baumgarten & Kamrin, 2019). However, the weakly compressible assumption encounters three distinct problems (Li *et al.*, 2014; Zhang *et al.*, 2017): (a) the critical time step of explicit time integration is limited by the virtual bulk modulus; (b) the free surface is not explicitly tracked, and hence pressure boundary conditions on the free surface cannot be imposed accurately; and (c) fluid material points suffer from significant pressure oscillations. To tackle the above-mentioned limitations, the fluid phase in this study is simulated using incompressible MPM (Zhang *et al.*, 2017). In the incompressible fluid model, the velocity field must satisfy the divergence free condition shown as follows

$$\nabla \cdot \mathbf{v}_f = 0 \quad (9)$$

The pore fluid pressure can be computed by solving equations (6) and (9) with the operator splitting method (Zhang *et al.*, 2017).

The deviatoric stress of the fluid phase is computed by assuming Newtonian rheology with dynamic viscosity  $\eta_f$  (Iverson & George, 2014) and considering the influences of the solid volume fraction given as follows (Einstein, 1906)

$$\mathbf{T}_f = \eta_f \left( 1 + \frac{5}{2} \phi \right) [\nabla \mathbf{v}_f + (\nabla \mathbf{v}_f)^T] \quad (10)$$

**Solid phase: shear rate-dependent non-associated Drucker–Prager yield criterion.** In debris flow–structure interaction, an elastic–perfectly plastic constitutive model with Mohr–Coulomb or Drucker–Prager failure criterion is generally used for the solid phase (Ceccato *et al.*, 2018; Ng *et al.*, 2018, 2020b; Cuomo *et al.*, 2021). However, these models cannot capture the loss of grain contact stresses when solid concentration is low (Guazzelli & Pouliquen, 2018). Moreover, these models usually have constant internal friction and dilation angles, which cannot capture the shear rate-dependent internal friction (GDR MiDi, 2004; Jop *et al.*, 2006) and the evolution of dilatancy with solid fraction (Fern & Soga, 2016). To tackle the above-mentioned limitations, a modified constitutive model proposed by Baumgarten & Kamrin (2019) is implemented in this study.

Figure 2 shows the yield surfaces of the implemented constitutive model,  $f_{\text{compaction}}$  and  $f_{\text{shear}}$ . The shear rate-dependent yield surfaces  $f_{\text{compaction}}$  and  $f_{\text{shear}}$  encapsulate the grains' response, evolving from shear rate-independent quasi-static frictional regime to shear rate-dependent dynamic frictional and collisional regimes (Pouliquen & Forterre, 2009).

Yield surface  $f_{\text{compaction}}$  (Baumgarten & Kamrin, 2019) depicts the relationship between the solid fraction, confining pressure and shear rate. Critical solid fraction ( $\phi_m$ ) describes the minimum solid fraction required to sustain prolonged granular contact (frictional behaviour), below which the granular contact is dominated by binary collisions between grains (collisional). During steady-state shearing, the equilibrium solid fraction ( $\phi_{\text{eq}}$ ) is shear rate-dependent (Amarsid *et al.*, 2017) and is given by

$$\phi_{\text{eq}} = \frac{\phi_m}{1 + aI_m} \quad (11)$$

where  $a$  is a material parameter;  $I_m$  is the mixed inertial number, defined as follows

$$I_m = \sqrt{I^2 + 2I_v} \quad (12)$$

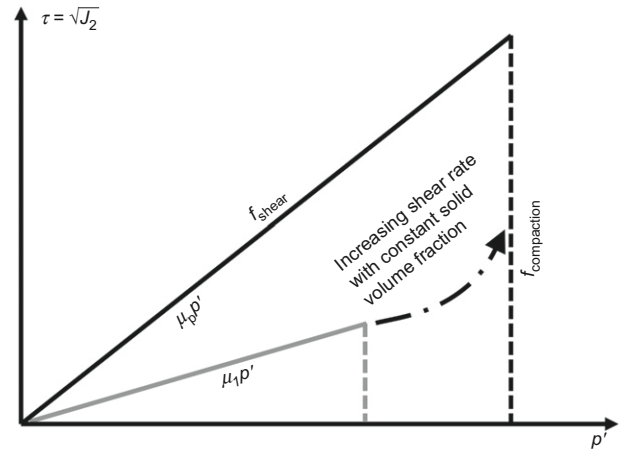


Fig. 2. Yield surfaces of the solid-phase constitutive model

where  $I$  is inertial number and  $I_v$  is viscous number, expressed as follows

$$I = \dot{\gamma}^p d \sqrt{\rho_s / p'} \quad (13)$$

$$I_v = \eta_f \dot{\gamma}^p / p' \quad (14)$$

where  $\dot{\gamma}^p$  is the equivalent plastic shear strain rate of the solid phase;  $p'$  is the mean effective stress of the solid phase;  $d$  is the diameter of solid particles; and  $\eta_f$  is the fluid viscosity.

Combining equations (11)–(14), the yield surface  $f_{\text{compaction}}$  is obtained as follows

$$f_{\text{compaction}} = g(\phi) p' - (a\phi)^2 [(\dot{\gamma}^p)^2 d^2 \rho_s + 2\eta_f \dot{\gamma}^p] \quad (15)$$

with

$$g(\phi) = \begin{cases} (\phi_m - \phi)^2 & \text{if } \phi < \phi_m \\ 0 & \text{if } \phi \geq \phi_m \end{cases} \quad (16)$$

The yield surface  $f_{\text{shear}}$  is defined as follows

$$f_{\text{shear}} = \sqrt{J_2} - \mu_p p' \quad (17)$$

where  $J_2$  is the second invariant of the deviatoric stress tensor and  $\mu_p$  is the total friction coefficient of the solid phase, expressed as follows

$$\mu_p = \mu_1 + \frac{\mu_2 - \mu_1}{1 + b/I_m} + \frac{5}{2} \left( \frac{\phi I_v}{a I_m} \right) \quad (18)$$

where  $b$  is a model parameter;  $\mu_1$  is the static friction coefficient; and  $\mu_2$  is the limiting value of maximum friction coefficient in  $\mu(I)$  rheology (GDR MiDi, 2004; Jop *et al.*, 2006); the third term on the right-hand side of equation (18) is the hydrodynamic contribution (Boyer *et al.*, 2011).

By defining the two yield surfaces in shear and compaction, the admissible stress state and plastic strain of the solid phase can be obtained. The plastic shear strain  $\gamma^p$ , plastic expansion  $\varepsilon_{vc}^p$  and plastic compaction  $\varepsilon_{vc}^p$  can be obtained by solving the equations below

$$\begin{cases} f_{\text{compaction}} \leq 0, & \varepsilon_{vc}^p \geq 0, & f_{\text{compaction}} \varepsilon_{vc}^p = 0 \\ f_{\text{shear}} \leq 0, & \gamma^p \geq 0, & f_{\text{shear}} \gamma^p = 0 \end{cases} \quad (19)$$

The plastic potential function corresponding to the yield surface  $f_{\text{shear}}$  is expressed as follows

$$P_{\text{shear}} = \sqrt{J_2} - \beta p' \quad (20)$$

where

$$\beta = K_4(\phi - \phi_{eq}) \quad (21)$$

where  $\beta$  is a state-dependent dilation angle, depending on the solid fraction and shear rate;  $K_4$  is a model parameter.  $\beta$  governs the plastic volumetric strain induced by the plastic shear strain (Pailha & Pouliquen, 2009; Iverson & George, 2014). In this study, the term  $(\phi - \phi_{eq})$  is updated at every time step to calculate the volumetric strain due to plastic shear strain.

**Inter-phase drag force.** The inter-phase drag force is obtained by considering the relative velocity between the two phases (Iverson & George, 2014; Bandara & Soga, 2015; Baumgarten & Kamrin, 2019). The volume-averaged inter-phase drag force is defined as follows (Van der Hoef *et al.*, 2005)

$$\mathbf{f}_d = \frac{18\phi(1-\phi)\eta_f}{d^2} \hat{\mathbf{F}}(\mathbf{v}_s - \mathbf{v}_f) \quad (22)$$

where  $\hat{\mathbf{F}}$  is a function of the solid fraction and grain Reynolds number. More details can be found in the paper by Van der Hoef *et al.* (2005).

**Model parameters in parametric study.** Material parameters used in the two-phase model and equivalent fluid model for parametric study are summarised in Table 1. In the two-phase model, the solid particles are assumed to be mono-dispersed in fluid (Fang *et al.*, 2022). The diameter of the solid particles is 1 mm based on typical sand particles (Iverson & George, 2014). The friction coefficient  $\mu_1$  is equal to 0.49 (internal friction angle  $\approx 31^\circ$ ), and shear rate-dependent parameters ( $a$ ,  $b$ ,  $\mu_2$ ) used in the numerical model are referenced from Baumgarten & Kamrin (2019). The initial solid fraction of flow material is considered to be equal to the critical solid volume fraction  $\phi_m$  of 0.56 (George & Iverson, 2014). The fluid phase is assumed to be water, with a viscosity equal to 0.001 Pa s.

#### Boundary conditions

For the two-phase model, the interfaces of the fluid phase on slope and rigid barrier are free-slip, meaning only the velocity normal to the boundary is set to be zero (Zhang *et al.*, 2017). The contact forces of the solid phase on slope and barrier are governed by Coulomb friction law with an interface friction  $\mu_{bed}$  coefficient equal to 0.4.

#### MPM model set-up and simulation plan

Figure 3 shows a schematic representation of the numerical simulation set-up used in this study. The debris flow–barrier interaction and the resulting overflow and landing are modelled using a two-dimensional (2D) plane-strain approximation (Trujillo-Vela *et al.*, 2020; Ng *et al.*, 2020b; Cuomo *et al.*, 2021). A sensitivity analysis has been carried out to ensure the mesh size is sufficiently fine to obtain reasonable impact forces. Details of the mesh sensitivity analyses are provided in Appendix 1. A fixed volume of debris mixture with initial aspect ratio of  $L_D/H_D \approx 8$  is set at the top of an inclined channel and released by way of dam break. A flow volume of 500 m<sup>3</sup> is modelled for this study by assuming a typical channel width of 10 m (Kwan, 2012). The inclination of the slope is 20°, which is typical in Hong Kong (Kwan *et al.*, 2015). Two barriers are modelled with a constant height, twice the maximum flow depth ( $h_{flow}$ ), to facilitate overflow and examine a worse scenario of overflow and landing kinematics (Ng *et al.*, 2018).

**Table 1. Parameters in two-phase and equivalent fluid models**

Parameter	Value		Unit
	Two-phase model	Equivalent fluid model	
	Solid phase		
Young's modulus, $E$	10	10	MPa
Poisson's ratio, $\nu$	0.3	0.3	—
Static friction coefficient, $\mu_1$ ( $\mu^{\text{eq}}$ )	0.49	0.27	—
Solid density, $\rho_s$	2650	1924	kg/m <sup>3</sup>
Dilatancy parameter, $K_4$	4.7	0	—
Limiting friction coefficient, $\mu_2$	1.4	—	—
Solid particle diameter, $d$	1	—	mm
$\mu(I)$ parameter, $a$	1.23	—	—
$\mu(I)$ parameter, $b$	0.31	—	—
Critical solid fraction, $\phi_{\text{m}}$	0.56	—	—
	Fluid phase		
Fluid density, $\rho_{\text{f}}$	1000	—	kg/m <sup>3</sup>
Fluid viscosity, $\eta_{\text{f}}$	$1 \times 10^{-3}$	—	Pa s
	Boundary		
Basal friction coefficient, $\mu_{\text{bed}}$ ( $\mu_{\text{bed}}^{\text{eq}}$ )	0.4	0.19	—

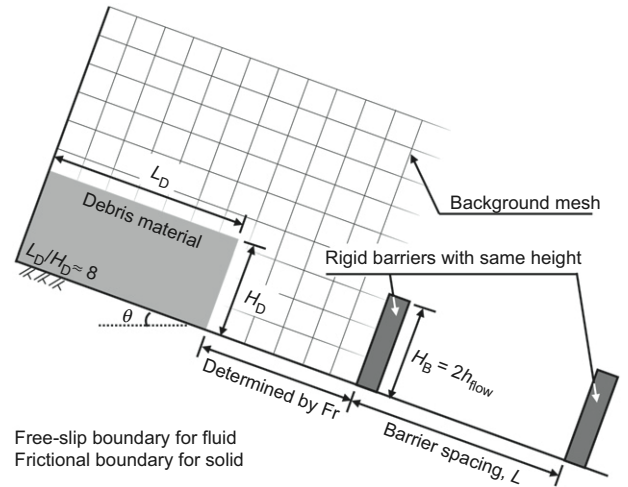


**Fig. 3. Schematic representation of simulation set-up (figure drawn not to scale)**

The Froude number ( $Fr$ ) of the flow at the barrier location is used to characterise the flow and determine the barrier location. The flow dynamics of free surface flows are distinguished using the Froude number based on the relative contribution of inertial force over gravitational force. The  $Fr$  is calculated by using the maximum flow velocity  $v_{flow}$  and the flow depth  $h_{flow}$  at the barrier location in a free-flow condition (without barrier)

$$Fr = \frac{v_{flow}}{\sqrt{\|g\| h_{flow} \cos \theta}} \quad (23)$$

$Fr < 1$  represents flows that are in the subcritical regime, whereas  $Fr > 1$  shows that the flows are in the supercritical regime. The Froude number of natural debris flows can range

from 0.5 to 7.6 (Hübl *et al.*, 2009). In this study, flows with Fr of 2, 4 and 6 are modelled by shifting the location of the first barrier.

Simulations without barriers are first conducted to obtain the flow velocity and depth along the slope under free-flow conditions. The location of the first barrier is determined according to the target Fr. Subsequently, the simulations with the first barrier are conducted to induce overflow and obtain the flow velocity and depth after landing. Finally, dual barriers are set up to obtain the impact force on the second barrier with different barrier spacings. Details of the simulation plan are summarised in Table 2.

#### Simulations with equivalent fluid method for comparison

To emphasise the importance of the two-phase model, an equivalent fluid model (Gao *et al.*, 2017; Kwan *et al.*, 2019; Zhao *et al.*, 2020; Vicari *et al.*, 2022) is also adopted to compare the computed results from the two-phase model. In the equivalent fluid method, two-phase debris flow is simplified as a single-phase frictional material with reduced internal and basal friction angles. A Coulomb frictional model is used rather than a Newtonian or non-Newtonian fluid rheological model to capture stress dependency in debris flow (Iverson, 2003). Therefore, the equivalent fluid model in this paper considers only the solid phase material points.

The numerical simulation set-up is the same as that of the two-phase model. The parameters for the equivalent fluid model are calibrated by comparing with the two-phase model results of: (a) the flow depth and velocity at different positions in free-flow conditions (i.e. without any barrier); (b) the peak impact force on the first barrier when Fr = 2, 4 and 6. The equivalent internal friction coefficient  $\mu^{\text{eq}}$  is

calibrated as 0.27 and the equivalent bed friction coefficient  $\mu_{\text{bed}}^{\text{eq}}$  is calibrated as 0.19 (as shown in Table 1). The smaller value of equivalent bed friction coefficient  $\mu_{\text{bed}}^{\text{eq}}$  compared with that adopted in the two-phase model is because the boundary frictional force is calculated based on the total stress rather than the effective stress of the flow (Iverson *et al.*, 2010).

Ideally, constant volume undrained conditions of debris mixtures are captured with a Poisson's ratio of 0.5 to model bulk incompressibility. However, it should be noted that the Young's modulus and Poisson's ratio in the equivalent fluid model are the same as those of the solid phase in a two-phase model. These sets of model parameters represent a compromise between computational efficiency and relative error in simulation results to simulate equivalent fluid material with negligible compressibility. The influence of artificial compressibility of the material on simulation results can be estimated by relative density variation  $\delta$  (Monaghan, 1994; Li *et al.*, 2014), which is expressed as follows

$$\delta = \frac{\|\mathbf{v}\|^2}{\{E(1-\nu)/[\rho(1-2\nu)(1+\nu)]\}} \quad (24)$$

where  $\|\mathbf{v}\|$  is the magnitude of the impact velocity on a barrier. With the decrease of  $\delta$ , the compressibility decreases. Simulation results by Dong *et al.* (2017) show that the peak impact pressure from undrained submarine debris flow on a pipeline increases by approximately 4%, when  $\delta$  decreases from 2.5% to 0.3%. Sensitivity analysis by Ceccato & Simonini (2016) shows that when  $\delta < 22.9\%$ , increasing Poisson's ratio in the elasto-plastic model (corresponding to decrease of  $\delta$ ) has trivial effects on the impact force. Since the  $\delta$  calculated using the current parameters in the equivalent fluid model (i.e.  $E = 10$  MPa and  $\nu = 0.3$ ) is 2.3%,  $E$  and  $\nu$

**Table 2. Simulation plan**

Simulation ID		Froude number Fr, at first barrier	Normalised barrier spacing, $L/x_i$	Notes
Two-phase model	Equivalent fluid model			
C_T	C_E	—	—	Control run without barrier
Fr2S_T	Fr2S_E	2	—	Single barrier
Fr2D1.5_T	Fr2D1.5_E		1.5	Dual barriers with same height
Fr2D2.0_T	Fr2D2.0_E		2.0	
Fr2D2.5_T	Fr2D2.5_E		2.5	
Fr2D3.0_T	Fr2D3.0_E		3.0	
Fr2D3.5_T	Fr2D3.5_E		3.5	
Fr2D4.0_T	Fr2D4.0_E		4.0	Single barrier
Fr2D4.5_T	Fr2D4.5_E		4.5	
Fr2D5.0_T	Fr2D5.0_E		5.0	
Fr4S_T	Fr4S_E	4	—	Dual barriers with same height
Fr4D1.5_T	Fr4D1.5_E		1.5	
Fr4D2.0_T	Fr4D2.0_E		2.0	
Fr4D2.5_T	Fr4D2.5_E		2.5	
Fr4D3.0_T	Fr4D3.0_E		3.0	
Fr4D3.5_T	Fr4D3.5_E		3.5	Single barrier
Fr4D4.0_T	Fr4D4.0_E		4.0	
Fr4D4.5_T	Fr4D4.5_E		4.5	
Fr4D5.0_T	Fr4D5.0_E		5.0	
Fr6S_T	Fr6S_E	6	—	Dual barriers with same height
Fr6D1.5_T	Fr6D1.5_E		1.5	
Fr6D2.0_T	Fr6D2.0_E		2.0	
Fr6D2.5_T	Fr6D2.5_E		2.5	
Fr6D3.0_T	Fr6D3.0_E		3.0	
Fr6D3.5_T	Fr6D3.5_E		3.5	Single barrier
Fr6D4.0_T	Fr6D4.0_E		4.0	
Fr6D4.5_T	Fr6D4.5_E		4.5	
Fr6D5.0_T	Fr6D5.0_E		5.0	



adopted from the two-phase model are considered to be reasonable in this study.

#### VALIDATION OF TWO-PHASE MPM MODEL

The MPM model implemented in this study is calibrated with experimental data for two-phase flow from this study and data for dry sand and water flows reported by Ng *et al.* (2020b, 2022). In this study, a two-phase flow with a mass of 30 kg composed of Toyoura sand ( $d_{50} \approx 0.2$  mm) at 36% solid volume fraction and water is used. The mixture is prepared in the storage container of a 0.2 m wide and 5 m long flume. An electric mixer is used to stir the sand and water mixture. The flume is then inclined to  $26^\circ$ . The gate of the container is opened to initiate a dam break. The debris material flowed down the channel and impacted a 0.1 m high barrier, 0.8 m away from the container gate. For the dry sand experiment (Ng *et al.*, 2020b), Leighton Buzzard fraction C sand with a particle size around 0.6 mm is used. The barrier height is 0.5 m to avoid overflow and the flume is inclined to  $23^\circ$ . For the experiment with water (Ng *et al.*, 2022), the barrier height is 0.1 m to facilitate overflow and the flume is inclined to  $26^\circ$ . The size of the regular background mesh is 2.5 mm, and 16 material points are initially generated for each phase in the mixture, dry sand or water. The parameters shown in Table 1 are used for the simulations, except the solid particle diameters ( $d = 0.2$  mm for sand in mixture flow and  $d = 0.6$  mm for dry sand flow).

#### Numerical modelling procedures

When modelling dry granular flow, material points of 30 kg of dry sand are generated in the storage container with top surface parallel to the flume bed (Ng *et al.*, 2020b). The direction of gravity is set to reach a bed inclination of  $23^\circ$ . After the total kinetic energy of the material points drops to  $10^{-6}$  kJ, the flow material is released by opening the gate of the storage container to initiate a dam break.

When modelling water and sand–water flows, the fluid material points are generated in the storage container with a horizontal surface to replicate the physical test conditions. For the sand–water flows, after generating fluid material points, the solid phase material points are uniformly distributed in fluid material points to model the initially well-mixed condition in physical tests. The direction of gravity is set to reach a bed inclination of  $26^\circ$ . Finally, the flow material is released by opening the gate of the storage container.

#### Validation of flow kinematics

Figure 4 shows a comparison between the observed and computed kinematics of a sand–water mixture impacting against a rigid barrier. At time  $t = 0.0$  s, the observed and computed flows start to impact the first barrier. The front velocity of 2.5 m/s is calculated based on the time taken by the flow front to travel a distance of 50 mm before impacting the barrier. The computed flow has a front velocity of 2.6 m/s, comparatively similar to the measured value. At time  $t = 0.2$  s, a jet-like run-up is observed in both the physical test and the computed result. The flow front in both the physical test and computed result launches at an angle of  $64^\circ$  to the horizontal plane. At time  $t = 0.4$  s, a stagnant dead zone forms behind the barrier and results in a relatively stable launching angle of overflow at  $53^\circ$  to the horizontal plane. At  $t = 2.0$  s, the incoming material tends to cease, and a part of the sand–water mixture is retained behind the barrier. Similar impact and overflow kinematics are found in both computed and experimental flows. This suggests that the

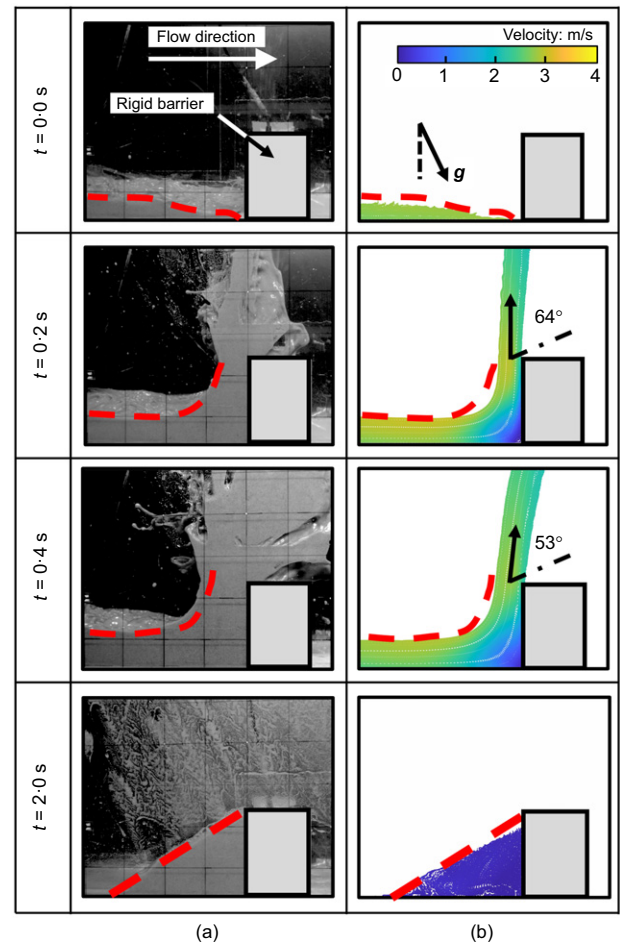


**Fig. 4.** Comparison of impact kinematics against rigid barrier (sand–water mixture, solid volume fraction = 0.36, present study): (a) physical test; (b) computed results. A full-colour version of this figure can be found on the ICE Virtual Library ([www.icevirtuallibrary.com](http://www.icevirtuallibrary.com))

two-phase MPM formulation used in this model can reliably capture the flow kinematics of two-phase flows.

#### Validation of impact force

Figure 5 shows a comparison of computed and measured time histories of impact force on the first barrier for dry sand, water and two-phase flows. After 0.5 s from impact, the impact force for dry sand flow gradually increases to a static load of 50 N, which is also the maximum load. For water and two-phase flows, the peak impact load is larger than that of the dry sand flow, and the maximum load is dynamic and occurs during run-up and overflow. The impact loads for water and two-phase flows after the peak drop to the values of static force, which is nearly zero due to the small amount of retention volume. The two-phase MPM in this study shows reasonable agreement with the measured and the computed impact forces.

The MPM model is validated by kinematics and the dynamics of dry sand, water and two-phase flows impacting a rigid barrier. The simulation results for three different flow types validate the incompressible fluid phase model, the solid phase constitutive model and the two-phase interaction model. Therefore, this validated MPM model is used for a parametric study (Table 2) by increasing the flow volume to  $500 \text{ m}^3$  to investigate the overflow and landing dynamics to cater to the design of multiple barriers.

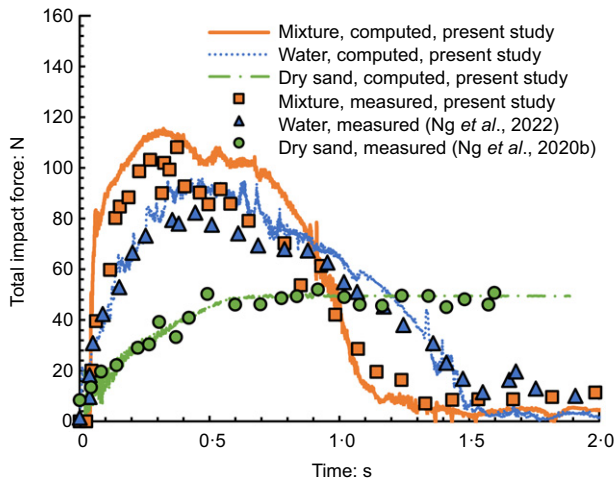


Fig. 5. Comparison of total impact forces on rigid barrier between measured and computed results. A full-colour version of this figure can be found on the ICE Virtual Library ([www.icevirtuallibrary.com](http://www.icevirtuallibrary.com))

## INTERPRETATION OF PARAMETRIC STUDY RESULTS

### Computed overflow and landing kinematics of two-phase debris flow

To reveal the overflow and landing mechanisms of two-phase flows, the flow kinematics of two extreme conditions with  $Fr = 2$  and  $Fr = 6$  are analysed. Fig. 6 shows the computed overflow and landing kinematics during the impact of the flow with  $Fr = 2$  against the first rigid barrier. Both the horizontal and vertical axes are length scales normalised by the flow depth. The contour plots show the velocity field during the impact. The launch trajectory calculated using equation (3) is also shown, assuming launch velocity  $v_{launch}$  is equal to the maximum flow velocity at the first barrier in the free-flow condition  $v_{flow}$ . By doing so, the interface friction angle of two-phase flow is assumed to be  $0^\circ$  in equation (3) and the top surface of the dead zone behind the barrier is assumed to be horizontal, following the design recommendations by Ng *et al.* (2020a). Consequently, the kinetic energy loss of incoming flow due to frictional shearing with the dead zone is assumed to be zero and run-up does not consume any kinetic energy of incoming flow. Equation (3) also assumes that the launch angle  $\theta_{launch}$ , which is the angle between the launch velocity and the horizontal, is  $0^\circ$  for simplicity. To evaluate equation (3), the computed and recommended  $v_{launch}$  and  $\theta_{launch}$  are compared.

For  $Fr = 2$ , the flow starts to impact the barrier at  $t = 0.0$  s and piles up to the crest of the barrier at  $t = 0.7$  s, with a dead zone formed behind the barrier (Fig. 6(a)). From  $t = 1.3$  s to  $2.3$  s (Figs 6(b) and 6(c)), the flow overflows with a launch velocity of  $2.1$  m/s and launch angle of  $2^\circ$  and lands on the slope with a maximum landing distance  $x_i$ . The computed  $x_i$  is much less than that predicted by equation (3), which assumes  $v_{launch} = v_{flow} = 7.4$  m/s. After the flow lands at  $t = 4.3$  s (Fig. 6(d)), the dead zone keeps enlarging and the top surface of the dead zone is inclined with the horizontal. The incoming flow continuously overflows from the crest of the barrier, and the landed debris propagates downslope with a frontal velocity of  $8.7$  m/s. Although the assumption in equation (3) for the launch angle of  $0^\circ$  is reasonable compared to the computed value of  $2^\circ$  at  $t = 2.3$  s, a significant difference is observed for the launch velocity. The computed launch velocity ( $2.1$  m/s) is greatly overestimated by taking  $v_{flow}$  ( $7.4$  m/s) as the launch velocity in equation (3), due to the assumption of a zero-friction angle

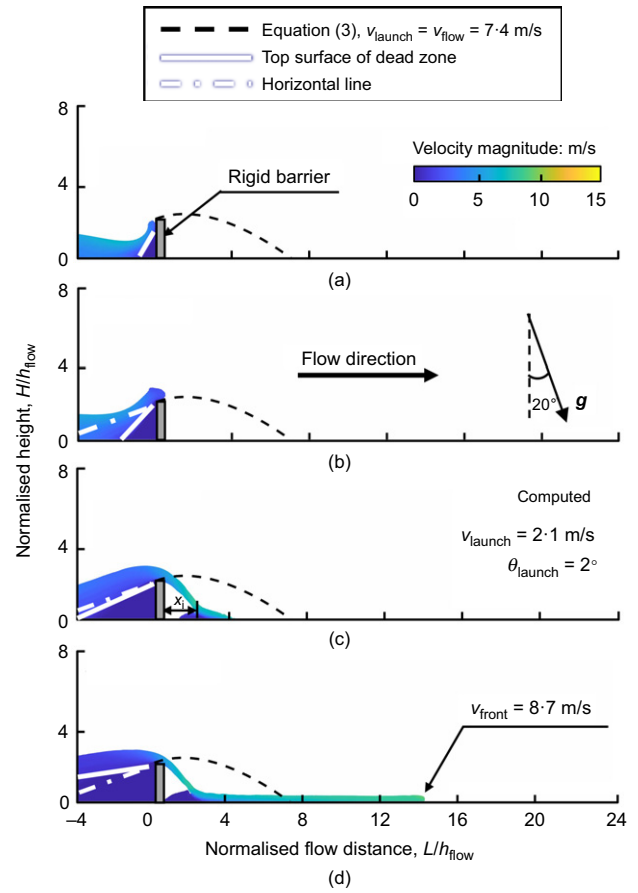


Fig. 6. Computed overflow and landing kinematics of  $Fr = 2$  for: (a)  $t = 0.7$  s; (b)  $t = 1.3$  s; (c)  $t = 2.3$  s; (d)  $t = 4.3$  s

for two-phase flows. Computed results reveal that the flow kinetic energy is mainly dissipated by the friction between solid particles, because  $\theta_{launch} = 2^\circ$  when the debris lands at a maximum distance. Therefore, the kinetic energy loss due to friction should be considered to obtain the launch velocity and the landing distance.

Similarly, Fig. 7 shows the computed overflow and landing kinematics during flow-barrier interaction when  $Fr = 6$ . The horizontal and vertical axes represent the normalised flow distance and normalised height, which are consistent with Fig. 6. The launch trajectory using equation (3) ( $v_{launch} = v_{flow} = 11.3$  m/s) is also shown for comparison. The flow starts to impact the barrier at  $t = 0.0$  s and a jet-like run-up occurs along with the formation of the dead zone at  $t = 0.7$  s (Fig. 7(a)). Compared with the pile-up for  $Fr = 2$  (Figs 6(a)–6(c)), the jet-like run-up for  $Fr = 6$  is caused by the high Froude number. From  $t = 1.3$  s to  $2.3$  s (Figs 7(b) and 7(c)), the incoming flow launches with a relatively stable velocity ( $8.1$  m/s) and angle ( $34^\circ$ ). The dead zone remains essentially static until  $t = 4.3$  s (Fig. 7(d)), contrasting with the enlarging dead zone observed for  $Fr = 2$  (Figs 6(b)–6(d)). This implies that the higher inertial force of the flow leads to less energy dissipation and the subsequent flow material is able to overflow atop the barrier. The stable top surface of the wedge-shaped dead zone is lower than the horizontal line and launches the incoming flow at an angle greater than zero. The computed maximum landing distance  $x_i$  is overestimated by equation (3) (with horizontal launch velocity of  $11.3$  m/s), albeit the calculated launch trajectory is lower than the computed one. The front velocity of landed debris for  $Fr = 6$  is  $15.3$  m/s (Fig. 7(d)) compared to  $8.7$  m/s for  $Fr = 2$  (Fig. 6(d)).

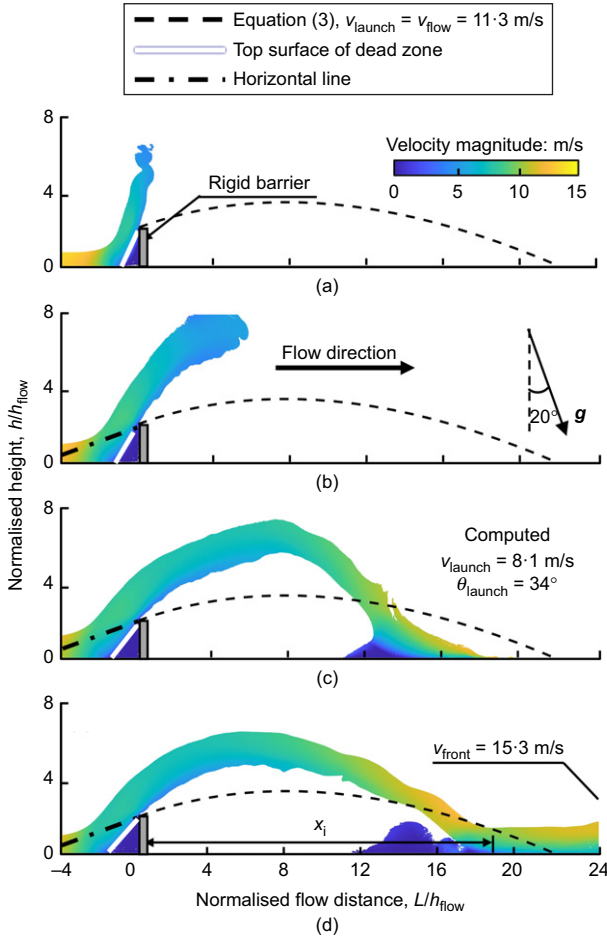


Fig. 7. Computed overflow and landing kinematics of  $Fr=6$  for: (a)  $t=0.7$  s; (b)  $t=1.3$  s; (c)  $t=2.3$  s; (d)  $t=4.3$  s

Compared to the flow with  $Fr=2$ , the assumption  $\theta_{\text{launch}} = 0^\circ$  in equation (3) is not consistent with the computed results for  $Fr=6$ . However, the calculated landing distance using equation (3) is still conservative. This is because the error in launch angle is compensated by the overestimated launch velocity (11.3 m/s). If the computed launch velocity (8.1 m/s) is used in equation (3) instead of the free-flow velocity (11.3 m/s), the calculated landing distance will be underestimated by 57%. Therefore, the assumption of  $\theta_{\text{launch}} = 0^\circ$  under high  $Fr$  should be treated with caution.

Similarly to the flow velocity, the normalised flow depth for  $Fr=2$  after landing is smaller than that for  $Fr=6$ . This is because the overflowing mass flux is greatly reduced when  $Fr=2$ . The mass flux of overflowing debris can be calculated by the flow depth at the barrier crest, launch velocity and density of the flow. The enlarging dead zone for  $Fr=2$  implies the mass flux of overflowing debris flow is lower than that in a free-flow condition ( $(\rho h_{\text{launch}} v_{\text{launch}} / \rho h_{\text{flow}} v_{\text{flow}}) \approx 0.3 < 1$ ). On the contrary, for  $Fr=6$ , the overflowing mass flux is approximately equal to that in the free-flow condition after the formation of a stable dead zone ( $(\rho h_{\text{launch}} v_{\text{launch}} / \rho h_{\text{flow}} v_{\text{flow}}) \approx 1$ ). Therefore, the flow depth after landing is larger than that for  $Fr=2$ . The differences in the size of dead zones in Figs 6 and 7 can be attributed to the difference in the ratio between the inertial force and gravitational force of the flow, as reflected by  $Fr$ . For  $Fr=2$ , the flow inertial force is only four times the gravitational force. The kinetic energy of the flow is spent as the flow piles up to the crest of the barrier. Energy is further dissipated by the friction between solid particles. However,

for  $Fr=6$ , the flow inertial force is 36 times the gravitational force. Therefore, only a small fraction of kinetic energy is used by the flow to overflow the barrier. The reduced energy dissipation for high Froude number flows implies that the overflow from the first barrier significantly influences the impact at the second barrier. The dynamic interaction of landing debris and subsequent barriers in a multiple barrier system should be considered, especially for high  $Fr$ .

Based on the two-phase model, the front velocities at  $t=4.3$  s of landed flow are 8.7 m/s and 15.3 m/s for  $Fr=2$  and  $Fr=6$ , respectively. However, frontal velocities of 7.8 m/s and 13.4 m/s, respectively, are computed by the equivalent fluid model (details are shown in Appendix 2). The equivalent fluid model ignores the solid–fluid interaction and overestimates the bed friction, and hence underestimates the flow velocities. The bed friction of two-phase flow can be calculated as follows

$$F_{\text{fric}} = \mu_{\text{bed}} \sigma'_{\text{bed}} = \mu_{\text{bed}} \sigma_{\text{bed}} (1 - \lambda) \quad (25)$$

where  $\sigma'_{\text{bed}}$  is the effective stress of the solid phase normal to the bed and  $\sigma_{\text{bed}}$  is the total stress normal to the bed.  $\lambda$  is the basal fluidisation ratio, which is defined as the ratio of basal pore fluid pressure and total stress, and is expressed as follows

$$\lambda = \frac{p_{\text{bed}}}{\sigma_{\text{bed}}} = \frac{p_{\text{bed}}}{(p_{\text{bed}} + \sigma'_{\text{bed}})} \quad (26)$$

where  $p_{\text{bed}}$  is the basal pore fluid pressure.  $\lambda$  represents the influence of basal pore fluid pressure on Coulomb friction.  $\lambda=0$  indicates that the effective stress of the flow is equal to the total stress, whereas  $\lambda=1$  indicates zero effective stress within the flow, and the friction between two-phase flow and bed vanishes. With the increase of  $\lambda$ , the energy dissipated by bed friction decreases, and hence the flow has a larger acceleration under gravity.  $\lambda$  may change due to landing-induced undrained loading and can affect the flow velocity after landing. The influence of  $\lambda$  on flow kinematics after landing is analysed in the next section.

#### Fluidisation ratio of flow after landing

Figure 8 shows the change in basal fluidisation ratio  $\lambda$  of the flow along varying flow distances  $L$  from the first barrier. Compared with the basal fluidisation ratio, the fluidisation ratio along the depth of landed flow varies by up to 10% due to the gradient of shear rate, therefore the basal fluidisation ratio is shown in Fig. 8. In this study, the  $\lambda$  is computed from the solid and fluid boundary forces of bed grids ( $F_{\text{bed}}^{\text{solid}}$  and  $F_{\text{bed}}^{\text{fluid}}$ , respectively), expressed as follows

$$\begin{aligned} \lambda &= \frac{p_{\text{bed}}}{(p_{\text{bed}} + \sigma'_{\text{bed}})} = \frac{p_{\text{bed}} \Delta x}{(p_{\text{bed}} + \sigma'_{\text{bed}}) \Delta x} \\ &= \frac{F_{\text{bed}}^{\text{fluid}}}{F_{\text{bed}}^{\text{fluid}} + F_{\text{bed}}^{\text{solid}}} \end{aligned} \quad (27)$$

where  $\Delta x$  is the mesh size along the bed. The flow distance  $L$  is normalised by the computed maximum landing distance  $x_i$ .  $L/x_i = 1.0$  represents the location of the maximum landing distance. Since the flows with different Froude numbers have a similar trend of fluidisation ratio, only the results of flow with  $Fr=4$  are shown. The  $\lambda$  values at  $t=3.6$  s, 4.0 s and 4.8 s are shown because flow propagates long enough to investigate the change of  $\lambda$  with flow distance. The average  $\lambda$  before impacting the barrier is around 0.6. Near the landing point ( $L/x_i = 1.0 \sim 1.2$ ),  $\lambda$  is smaller than 0.6, but increases with the flow distance.  $\lambda$  increases by up to 30% when  $L/x_i \approx 1.4$  and gradually decreases to 0.6 when  $L/x_i \approx 3.0$ .



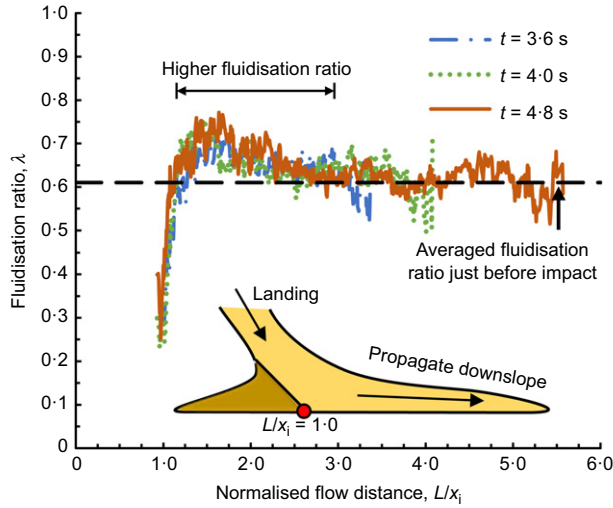


Fig. 8. Fluidisation ratio after landing for flow with  $Fr = 4$ . A full-colour version of this figure can be found on the ICE Virtual Library ([www.icevirtuallibrary.com](http://www.icevirtuallibrary.com))

Although  $\lambda$  is smaller than 0.6 near the landing point ( $L/x_i = 1.0 \sim 1.2$ ), an obvious increasing trend is observed with  $\lambda$  values higher than 0.6 after landing ( $L/x_i = 1.2 \sim 3.0$ ). Incoming flow continuously lands on the bed, resulting in similar trends of  $\lambda$  with the flow distance at these instances. The change of  $\lambda$  plays a key role in flow mobility (Iverson *et al.*, 2010); however, this cannot be captured by the equivalent fluid method. The bed friction in the equivalent fluid method is calculated based on an equivalent bed friction coefficient  $\mu_{bed}^{eq}$  and total stress normal to the bed as follows

$$F_{fric}^{eq} = \mu_{bed}^{eq} \sigma_{bed} \quad (28)$$

The change of fluidisation ratio  $\lambda$  can serve to enable the equivalent fluid model to capture friction between the two-phase flow and the bed. By equating the bed friction estimated by the equivalent fluid method (equation (28)) and the two-phase method (equation (25)), the following relation is obtained

$$\frac{F_{fric}^{eq}}{F_{fric}} = \frac{\mu_{bed}^{eq} (p_{bed} + \sigma'_{bed})}{\mu_{bed} \sigma'_{bed}} = \frac{\mu_{bed}^{eq}}{\mu_{bed}} \frac{1}{1 - \lambda} = 1 \quad (29)$$

$$\therefore \mu_{bed}^{eq} = \mu_{bed} (1 - \lambda)$$

With the increase of  $\lambda$  after landing (Fig. 8),  $\mu_{bed}^{eq}$  should be reduced for a distance of  $1.0 < L/x_i < 3.0$ . The reduced  $\mu_{bed}^{eq}$  lowers basal frictional dissipation and can increase the flow velocity as computed in the case of the two-phase model. To further explain the change of  $\lambda$ , the shear behaviour during landing is analysed in the next section.

#### Shear behaviour during landing

Figure 9 shows the shear rate fields corresponding to the varying time in Fig. 8 for flow with  $Fr = 4$  after landing. The flow distance normalised by the computed maximum landing distance,  $x_i$ , is shown in the abscissa. The ordinate shows the height normalised by the flow depth,  $h_{flow}$ . The shear rate,  $\dot{\gamma}^p$ , is the equivalent plastic shear strain divided by the computation time step. During landing, some of the flow material spreads upstream and deposits with a shear rate near 0 (Fig. 9(a)). At the same time, as the incoming landing material overrides the static debris, a large shear rate develops between the landing debris and the static deposit. The shear rate

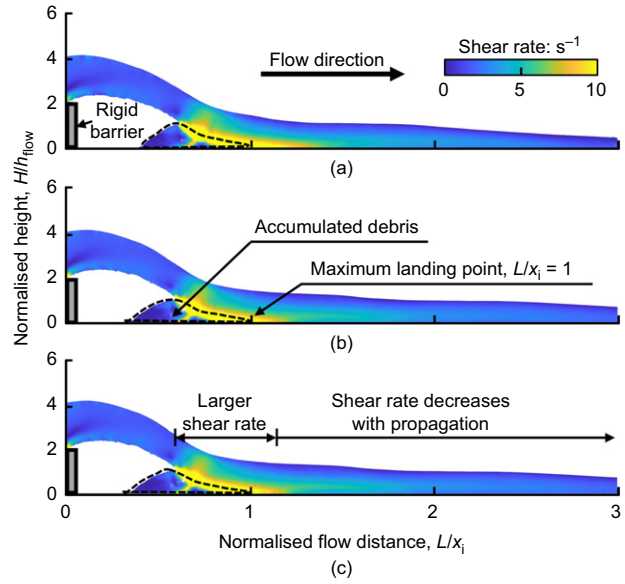


Fig. 9. Shear rate during landing for flow with  $Fr = 4$  for: (a)  $t = 3.6$  s; (b)  $t = 4.0$  s; (c)  $t = 4.8$  s

decreases along the propagation length ( $L/x_i > 1.2$ ), because the velocity difference between the bed and free surface reduces after landing. With the influx of more material (Figs 9(b) and 9(c)), the debris slightly accumulates to the upstream of the landing point ( $L/x_i \leq 1.0$ ). Similar trends of  $\dot{\gamma}^p$  at three instances (Fig. 9) cause similar distribution of the fluidisation ratio along the flow path (Fig. 8).

The changing shear rate causes the increase of fluidisation ratio shown in Fig. 8. The increase in shear rate induces a large internal friction coefficient  $\mu_p$  as indicated by equation (18), but a small equilibrium solid fraction  $\phi_{eq}$  as indicated by equations (11) and (12). With the increase of  $\dot{\gamma}^p$  near the landing point, the equilibrium solid fraction  $\phi_{eq}$  under shearing decreases and the solid phase tends to dilate (equation (21)). The dilation of the solid phase leads to a decrease of pore fluid pressure and a lower fluidisation ratio near the landing point ( $L/x_i = 1.0 \sim 1.2$ , Fig. 8). As the shear rate decreases along the propagation distance, the solid phase tends to compact due to increasing  $\phi_{eq}$ . The rapid increase of the solid fraction leads to an increase of pore fluid pressure, and hence the higher fluidisation ratio ( $L/x_i = 1.2 \sim 3.0$ , Fig. 8). The pore fluid pressure dissipates as the flow propagates downstream, and the fluidisation ratio decreases to the value in the free-flow condition without the barrier.

The inertial number  $I$  can be used to evaluate the importance of the shear rate-dependent characteristics in simulation. Based on the  $\dot{\gamma}^p$  and  $p'$  of solid material points,  $I$  is of the order of  $10^{-2}$ , in which shear rate-dependent characteristics should be considered (GDR MiDi, 2004). The shear rate-dependent constitutive model implemented in this study shows that the change of shear rate affects the dilation of the solid phase during landing. For two-phase debris flows, constitutive models with constant dilation angle may not capture the fluidisation ratio change during and after landing. The shear rate-dependent characteristics significantly affect the landing process with the increase of inertial number  $I$ , and should be considered in the numerical simulations to correctly capture the impact kinematics of debris flow against multiple barriers.

#### Flow velocity and depth after landing

After examining the changes of fluidisation ratios, the resulted flow velocity and depth after landing are discussed in

this section. Fig. 10 shows a comparison of flow velocities computed by the two-phase and equivalent fluid MPM models at different locations after landing ( $L/x_i > 1.0$ ). The normalised peak flow velocity at respective locations downstream of the first barrier is shown in the ordinate. The peak flow velocity is normalised by the velocity just after landing  $v_i$  with a velocity correction factor  $R = 1.0$  (equation (4)). Flow velocities for different  $Fr$  values are compared. The velocity after landing increases with the distance due to the flow reacceleration under gravity (Ng *et al.*, 2018). The velocity correction factor  $R = 1.0$  proposed by Ng *et al.* (2020a) underestimates the flow velocity after landing by up to 40% near the landing point ( $L/x_i = 1.5$ ) and 80% at a distance of  $L/x_i = 5.0$ . The underestimation of flow velocity is because the flow is simplified as a point mass and flow reacceleration after landing is neglected.

Although the flow propagation after landing is considered by the equivalent fluid method, the flow velocity estimated by the equivalent fluid method is also smaller than that predicted by the two-phase model. This is because the increase of the fluidisation ratio (Fig. 8) is not captured by the equivalent fluid method as explained earlier. The equivalent fluid-based mobility analysis (Kwan *et al.*, 2015) adopts an overestimated bed friction after landing, and hence the flow velocity is underestimated.

Figure 11 shows a comparison of flow depth computed by the two-phase and equivalent fluid models at different locations after landing. The flow depth is normalised by the maximum flow depth  $h_{flow}$  at the first barrier. Flow depths under different  $Fr$  values are also compared. When  $Fr = 2$ , the flow depth just after landing is much less than that of the free-flow condition, which can be attributed to the reduced mass flux as observed in Figs 6(b)–6(d). In contrast, when  $Fr \geq 4$ , the mass flux is approximately equal to that at the first barrier location in the free-flow condition. The mass of accumulated debris changes little (see Fig. 9), and hence  $\rho h_i v_i \approx \rho h_{launch} v_{launch} \approx \rho h_{flow} v_{flow}$ . The velocity just after landing  $v_i$  is less than  $v_{flow}$  at the first barrier in the free-flow condition ( $v_i/v_{flow} < 1.0$ ), due to the momentum redirection induced by the first barrier. Hence, based on mass conservation, the  $h_i/h_{flow}$  can be larger than 1.0. With the propagation after landing, the flow depth keeps decreasing under gravity. The equivalent fluid model predicts a conservative flow depth after landing. This may be attributed to the underestimation of flow velocity after landing by the equivalent fluid method, since the mass flux is approximately equal to that of the

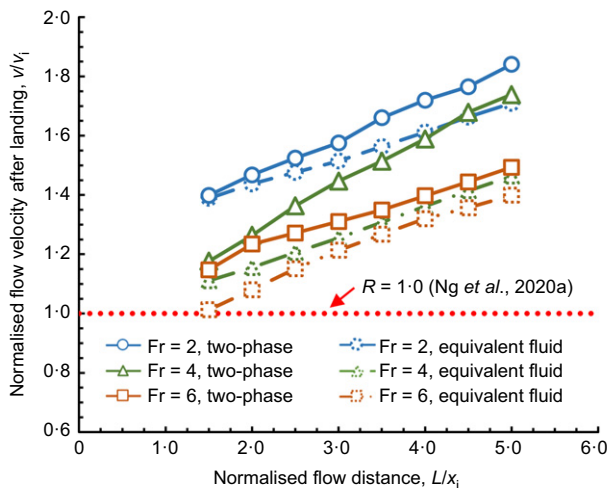


**Fig. 10.** Flow velocities after landing at different flow distances to the first barrier, computed by two-phase and equivalent fluid models

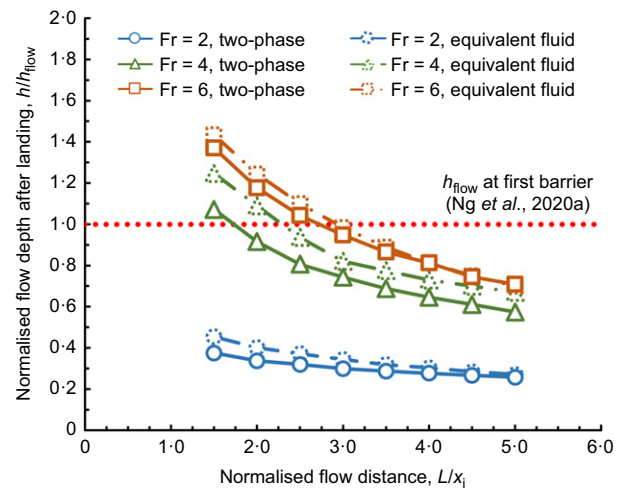


**Fig. 11.** Flow depths after landing at different flow distances to the first barrier, computed by two-phase and equivalent fluid models

two-phase model. The increased flow depth after landing suggests that, for flow with large Froude numbers ( $Fr \geq 4$  in this study), adopting the flow depth at the first barrier may not be conservative if the second barrier is installed at  $L/x_i < 2.0$ .

#### Impact force on the second barrier

After examining the flow velocity and depth after landing from the first barrier, the impact force on the second barrier is examined. Fig. 12 shows a comparison of impact force on the second barrier for different barrier spacings and Froude numbers computed by the two-phase and equivalent fluid models. The impact force is normalised by the recommended design force on the second barrier by Ng *et al.* (2020a) using equation (1) with  $\alpha$  and  $k$  equal to unity.

With the increase of barrier spacing, impact forces for flow with  $Fr = 2$  computed by both two-phase and equivalent fluid models decrease and keep constant when  $L/x_i > 3.0$ . In contrast, for flows with  $Fr = 4$  and 6, impact forces first decrease and then keep increasing as the barrier spacing increases. Impact forces are the smallest when  $L/x_i = 2.0$ . The impact force predicted by the equivalent fluid model has the same trends as the two-phase model, albeit with large underestimation. The impact force is underestimated by the equivalent fluid model because of the underestimated flow impact velocity (Fig. 10) on the second barrier location.

The reason for a larger impact force near the landing location ( $L/x_i = 1.5$  in the present study) is likely to be because the overflow energy cannot be effectively dissipated by way of the landing process as reported by Ng *et al.* (2018). If  $L/x_i$  is larger than a threshold value ( $L/x_i \approx 2.0$  in the present study), the impact force increases with the barrier spacing as more potential energy is converted to kinetic energy. However, for flow with a low Froude number ( $Fr = 2$  in the present study), the static force of retained debris is the key component of force acting on the subsequent barrier. The dynamic force is small because the flow depth is greatly reduced. Based on the recommended design impact force proposed by Ng *et al.* (2020a), the impact force can be underestimated by up to 50% when  $L/x_i = 5.0$  under  $Fr = 6$ . This is because the impact velocity is much larger than  $v_i$ , although the flow depth is overestimated.

The impact force predicted by the equivalent fluid method also underestimates the impact force on the second barrier, although the propagation after landing is considered. The

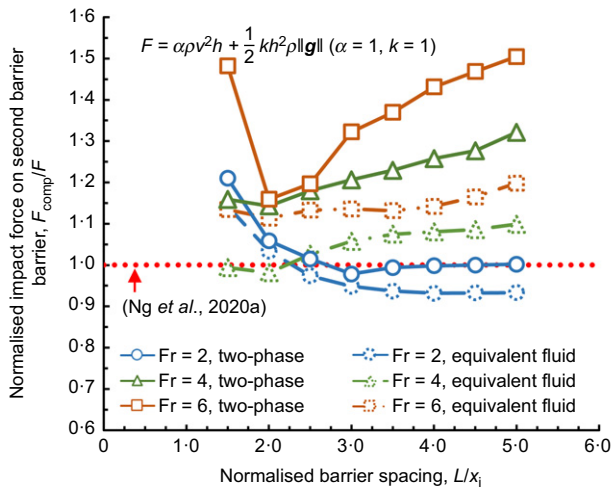


**Fig. 12. Impact force on the second barrier, computed by two-phase and equivalent fluid models**

discrepancy is mainly induced by the assumption of constant bed friction coefficient  $\mu_{bed}^{eq}$ . The increased fluidisation ratio (Fig. 8) leads to less energy dissipation after landing, and hence the flow velocity computed by the two-phase model is larger. Although the flow depth after landing is conservative in all cases from the equivalent fluid method (Fig. 11), the increased velocity plays a more important role in the impact force. The normalised impact force on the second barrier is underestimated by the equivalent fluid method by up to 25% for all cases. As such, correct estimation of the flow velocity after landing with a two-phase model is of paramount importance in conservatively designing debris-resistant multiple barriers.

This study mainly focuses on the mechanisms of changes of flow velocity and flow depth after debris flow impacts the first barrier, overflows and lands on the slope. This is because the major challenge of estimating the impact force on the second barrier lies in correctly predicting the flow velocity and flow depth impacting the second barrier. By obtaining reliable flow velocity and flow depth, the impact force on the second barrier can be estimated using equation (1), which captures both the hydrodynamic and hydrostatic forces of debris flow and has been adopted in engineering practice (Jóhannesson *et al.*, 2009; Ng *et al.*, 2020a) and research (Armanini *et al.*, 2020; Fang *et al.*, 2022; Ng *et al.*, 2022).

It should be noticed that equation (1) adopts a combined hydrodynamic and hydrostatic approach to estimate the impact force of debris flow as a fluid while neglecting the shear strength of the flow. Previous studies (Randolph & White, 2012; Dong *et al.*, 2017, 2020) have revealed that the shear strength plays a non-trivial role in the impact force on a pipe fully engulfed by submarine landslides. The impact force due to the shear strength of the flow can be calculated as  $N_p c_u$ , where  $N_p$  is a resistance factor and  $c_u$  is the mobilised undrained shear strength. To estimate the influence of debris strength in this paper, it is assumed that the  $c_u$  is a product of rate-dependent friction coefficient ( $\mu_2$ ) and maximum effective stress of flow at the barrier location ( $\rho' \|g\| \cos \theta$ ).  $N_p$  equal to 0.5 is adopted from Dong *et al.* (2017, 2020) as the barrier height is double the flow depth. It is found that the debris strength term only contributes less than 10% of the total impact force. This small contribution to impact force is because of the large impact velocity ( $>7$  m/s) and a small value of  $N_p = 0.5$ . As such, the flow velocity and flow depth after landing play key roles in the variations of the dynamic and static impact forces on the second barrier. The term

' $N_p c_u$ ' is neglected in this study while comparing the computed results with the current design recommendation (Jóhannesson *et al.*, 2009; Ng *et al.*, 2020a). Nevertheless, the effects of shear strength on impact force may be dominant for debris flows on a gentle terrain where the flow velocity is usually small, and warrant further investigation.

In this study, only a single flow volume is used, which is representative of a typical design event in Hong Kong. Furthermore, the barrier height is kept constant at double the flow depth as recommended by Ng *et al.* (2018) to enhance overflow. It is acknowledged that the scale-dependent behaviour of debris flows directly corresponds to the initial debris flow volume (Iverson, 2015). Two competing influences tend to occur in terms of constitutive response. First, an increase in the flow depth for larger initial volume will result in a decrease of shear rate and increase of effective stress, and therefore a corresponding reduction of the mixed inertial number  $I_m$  (equation (12)) during landing. This reduction of  $I_m$  means a smaller dilatancy of the solid phase (equations (11) and (21)) during landing and consequently lower maximum fluidisation ratio after landing. In this scenario, the basal friction coefficient after landing tends to be higher, which is likely to reduce the flow velocity reaching the second barrier. Second, after landing, for larger flow depth excess pore fluid pressure is sustained for a longer time as the solid phase requires a longer time for consolidation. This sustained excess pore fluid pressure tends to reduce the effective stress and lower the basal friction coefficient after landing, which increases the flow velocity at the second barrier. The effects of these two competing dynamics induced by flow volume on the second barrier impact force should be further investigated.

## CONCLUSIONS

In this study, a fully coupled two-phase two-layer MPM with incompressible fluid phase is implemented. This MPM model is validated using physical flume test results of flow-barrier interaction of dry sand, water and sand-water mixture flows. The validated MPM model is then used to investigate the influence of Froude number and barrier spacing on the impact force on the second barrier for dual rigid barriers. The following key findings may be drawn from this study.

- Existing international design recommendations can underestimate the impact force of two-phase debris flow on the second barrier by up to 50% because they neglect the fluidisation ratio change and flow reacceleration after landing. The fluidisation ratio, which is the ratio of basal pore fluid pressure and total stress, increases by up to 30% after landing of overflow compared to the free-flow condition. Consequently, the flow impact velocity at the second barrier increases by up to 80%.
- The commonly adopted debris mobility models, which simplify the debris flow as an equivalent fluid, may be suitable for estimating a single barrier impact. However, this equivalent fluid model is unable to capture the decreased bed friction after landing of overflow and may lead to an underestimation of the impact force on the second barrier by up to 25%. A two-phase numerical model is therefore necessary for designing multiple barriers.
- The flow depth after landing can increase up to 40% compared with the flow depth impacting the first barrier when the Froude number  $Fr \geq 4$ . This is



because the mass flux of landing debris is approximately equal to that at the first barrier location in free-flow conditions – that is,  $\rho h_i v_i \approx \rho h_{\text{flow}} v_{\text{flow}}$ , where  $h$ ,  $v$  and  $\rho$  denote the flow depth, flow velocity and flow density, respectively, and subscripts ‘flow’ and ‘i’ represent the free-flow condition and after landing, respectively. Since the flow velocity after landing  $v_i$  is smaller than the free-flow velocity  $v_{\text{flow}}$  when  $L/x_i < 3$ , mass conservation results in  $h_i$  greater than  $h_{\text{flow}}$ .

- (d) As a relatively simple shear rate-dependent soil constitutive model is adopted, direct application of the findings to engineering practice should be treated with caution.

## ACKNOWLEDGEMENTS

The work described in this paper was supported by a grant from the Research Grants Council (RGC) of the Hong Kong Special Administrative Region (HKSAR), People’s Republic of China (project no. AoE/E-603/18). Sunil Poudyal and Aastha Bhatta gratefully acknowledge the support of Hong Kong PhD Fellowship Scheme (HKPFS) provided by the RGC of HKSAR, People’s Republic of China.

## APPENDIX 1. INFLUENCE OF MESH SIZE IN MPM ON IMPACT FORCE

Figure 13 shows the results of sensitivity analysis of background mesh size by comparing the computed total impact force on the barrier. A Cartesian background mesh is adopted in this study. A constant material point density of 16 material points per cell is maintained in both analyses. The barrier height-to-flow depth ratio is kept constant at 2.0 in all simulations. As such, the ratio between mesh size and barrier height is used to evaluate the influence of mesh size on the resolution of computed impact force (Dong *et al.*, 2017, 2020). By decreasing this ratio from 0.04 to 0.02, a difference of only 1% in peak impact force is obtained, as shown in Fig. 13. Therefore, a mesh size-to-barrier height ratio of 0.04 is used in this study.

## APPENDIX 2. PROPAGATION OF FLOW AFTER LANDING FOR TWO-PHASE MODEL AND EQUIVALENT FLUID MODEL

Figure 14 shows the flow after landing at  $t = 4.3$  s in two-phase and equivalent fluid models under  $\text{Fr} = 2$  (Fig. 14(a)) and  $\text{Fr} = 6$  (Fig. 14(b)). The flow propagates farther in the two-phase model

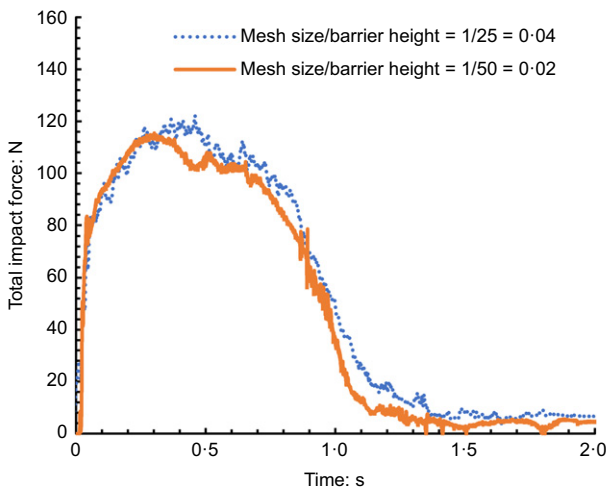


Fig. 13. Sensitivity analysis of mesh size on the computed impact forces during the validation of sand–water mixture case

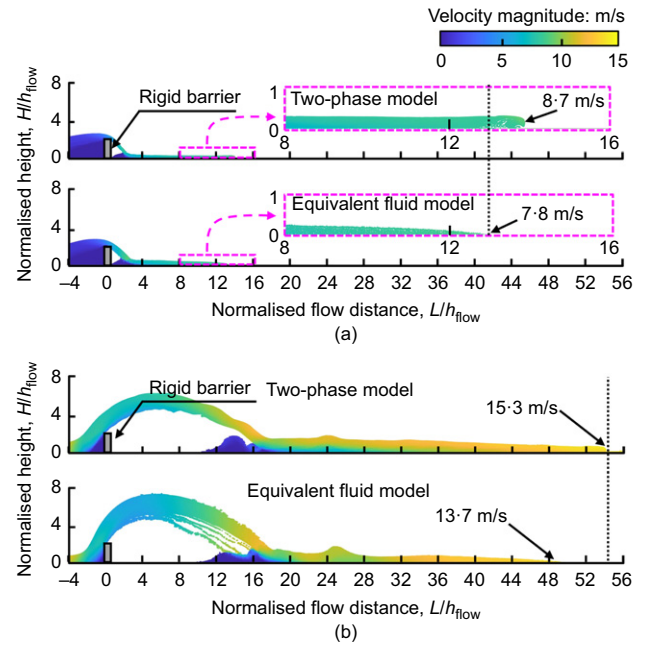


Fig. 14. Flow after landing at  $t = 4.3$  s in two-phase and equivalent fluid models: (a)  $\text{Fr} = 2$ ; (b)  $\text{Fr} = 6$

than the equivalent fluid model for both  $\text{Fr} = 2$  and  $\text{Fr} = 6$  due to the underestimation of flow velocity after landing predicted by the equivalent fluid model.

## NOTATION

$a, b, K_4$	dimensionless model parameters
$d$	solid particle diameter
$F, F_{\text{comp}}$	theoretical/computed impact force on barrier
$\bar{F}$	drag force coefficient
$F_{\text{fric}}, F_{\text{fric}}^{\text{eq}}$	bed friction in two-phase model and equivalent fluid model, respectively
$\text{Fr}$	Froude number
$\mathbf{f}_d$	interphase drag force vector
$\mathbf{g}$	vector of gravitational acceleration
$H_B$	barrier height
$h$	flow depth
$h_{\text{flow}}$	maximum flow depth at barrier location in free-flow conditions
$h_{\text{launch}}, h_i$	flow depth at barrier crest and just after landing, respectively
$I, I_m, I_v$	inertial number, mixed inertial number and viscous number, respectively
$J_2$	second invariant of solid-phase deviatoric stress
$p', p_f$	mean effective stress of solid phase and pore fluid pressure, respectively
$R$	velocity correction factor
$v$	flow velocity
$v_{\text{flow}}$	maximum flow velocity at barrier location in free-flow conditions
$v_{\text{launch}}, v_r, v_i$	velocity magnitude at barrier crest, just before landing and just after landing, respectively
$\mathbf{v}_s, \mathbf{v}_f$	velocity vector of solid phase and fluid phase, respectively
$x_i$	maximum landing distance
$\alpha, k$	dynamic and static impact coefficient, respectively
$\beta$	state-dependent dilation angle
$\gamma^p$	equivalent plastic shear strain
$\varepsilon_v^e, \varepsilon_v^c$	plastic expansion and compaction, respectively
$\eta_f$	dynamic viscosity of fluid phase
$\theta, \theta_{\text{launch}}$	slope angle and launch angle, respectively
$\lambda$	fluidisation ratio
$\mu_1, \mu_2$	static and limiting friction coefficient of solid phase, respectively



$\mu_{\text{bed}}, \mu_{\text{bed}}^{\text{eq}}$	bed friction coefficient in two-phase and equivalent fluid model, respectively
$\mu_{\text{p}}$	total friction coefficient of solid phase
$\rho, \rho_{\text{s}}, \rho_{\text{f}}$	density of mixture, solid and fluid, respectively
$\bar{\rho}_{\text{s}}, \bar{\rho}_{\text{f}}$	solid and fluid effective density, respectively
$\sigma_{\text{bed}}, \sigma'_{\text{bed}}$	total and effective bed normal stress, respectively
$\sigma'$	effective stress tensor of solid phase
$\mathbf{T}_{\text{f}}$	deviatoric stress tensor of fluid phase
$\phi, \phi_{\text{m}}, \phi_{\text{eq}}$	current, critical and equilibrium solid volume fraction, respectively

## REFERENCES

- Amarsid, L., Delenne, J. Y., Mutabaruka, P., Monerie, Y., Perales, F. & Radjai, F. (2017). Viscoinertial regime of immersed granular flows. *Phys. Rev. E* **96**, No. 1, 012901, <https://doi.org/10.1103/PhysRevE.96.012901>.
- Armanini, A., Rossi, G. & Larcher, M. (2020). Dynamic impact of a water and sediments surge against a rigid wall. *J. Hydraul. Res.* **58**, No. 2, 314–325, <https://doi.org/10.1080/00221686.2019.1579113>.
- ASI (Austrian Standards Institute) (2013). ONR 24801: Protection works for torrent control – static and dynamic actions on structures. Vienna, Austria: Austrian Standards Institute.
- Bandara, S. & Soga, K. (2015). Coupling of soil deformation and pore fluid flow using material point method. *Comp. Geotech.* **63**, 199–214, <https://doi.org/10.1016/j.compgeo.2014.09.009>.
- Baumgarten, A. S. & Kamrin, K. (2019). A general fluid–sediment mixture model and constitutive theory validated in many flow regimes. *J. Fluid Mech.* **861**, 721–764, <https://doi.org/10.1017/jfm.2018.914>.
- Boyer, F., Guazzelli, É. & Pouliquen, O. (2011). Unifying suspension and granular rheology. *Phys. Rev. Lett.* **107**, No. 18, 188301, <https://doi.org/10.1103/PhysRevLett.107.188301>.
- Ceccato, F. & Simonini, P. (2016). Granular flow impact forces on protection structures: MPM numerical simulations with different constitutive models. *Procedia Engng* **158**, 164–169, <https://doi.org/10.1016/j.proeng.2016.08.423>.
- Ceccato, F., Redaelli, I., di Prisco, C. & Simonini, P. (2018). Impact forces of granular flows on rigid structures: comparison between discontinuous (DEM) and continuous (MPM) numerical approaches. *Comput. Geotech.* **103**, 201–217, <https://doi.org/10.1016/j.compgeo.2018.07.014>.
- CGS (China Geological Survey) (2004). *Design code for debris flow disaster mitigation measures (DZ/T0239-2004)*. Beijing, China: China Geological Survey (in Chinese).
- Cui, P., Zeng, C. & Lei, Y. (2015). Experimental analysis on the impact force of viscous debris flow. *Earth Surf. Process. Landf.* **40**, No. 12, 1644–1655, <https://doi.org/10.1002/esp.3744>.
- Cuomo, S., Perna, A. D. & Martinelli, M. (2021). Material point method (MPM) hydro-mechanical modelling of flows impacting rigid walls. *Can. Geotech. J.* **58**, No. 11, 1730–1743, <https://doi.org/10.1139/cgj-2020-0344>.
- Dong, Y., Wang, D. & Randolph, M. F. (2017). Investigation of impact forces on pipeline by submarine landslide using material point method. *Ocean Engng* **146**, 21–28, <https://doi.org/10.1016/j.oceaneng.2017.09.008>.
- Dong, Y., Wang, D. & Randolph, M. F. (2020). Quantification of impact forces on fixed mudmats from submarine landslides using the material point method. *Appl. Ocean Res.* **102**, 102227, <https://doi.org/10.1016/j.apor.2020.102227>.
- Einstein, A. (1906). Calculation of the viscosity-coefficient of a liquid in which a large number of small spheres are suspended in irregular distribution. *Ann. Phys. Leipzig* **324**, No. 19, 286–306 (in German).
- Fang, J., Wang, L., Hong, Y. & Zhao, J. (2022). Influence of solid–fluid interaction on impact dynamics against rigid barrier: CFD–DEM modelling. *Géotechnique* **72**, No. 5, 391–406, <https://doi.org/10.1680/jgeot.19.P160>.
- Fern, E. J. & Soga, K. (2016). The role of constitutive models in MPM simulations of granular column collapses. *Acta Geotech.* **11**, No. 3, 659–678, <https://doi.org/10.1007/s11440-016-0436-x>.
- Gao, Y., Yin, Y., Li, B., Feng, Z., Wang, W., Zhang, N. & Xing, A. (2017). Characteristics and numerical runout modeling of the heavy rainfall-induced catastrophic landslide–debris flow at Sanxicun, Duijiangyan, China, following the Wenchuan Ms 8.0 earthquake. *Landslides* **14**, No. 4, 1361–1374, <https://doi.org/10.1007/s10346-016-0793-4>.
- GDR MiDi (2004). On dense granular flows. *Eur. Phys. J. E* **14**, No. 4, 341–365, <https://doi.org/10.1140/epje/i2003-10153-0>.
- George, D. L. & Iverson, R. M. (2014). A depth-averaged debris-flow model that includes the effects of evolving dilatancy. II. Numerical predictions and experimental tests. *Proc. R. Soc. A – Math. Phys.* **470**, No. 2170, 20130820, <https://doi.org/10.1098/rspa.2013.0820>.
- Guazzelli, É. & Pouliquen, O. (2018). Rheology of dense granular suspensions. *J. Fluid Mech.* **852**, 1–73, <https://doi.org/10.1017/jfm.2018.548>.
- Hübl, J., Suda, J., Proske, D., Kaitna, R. & Scheidl, C. (2009). Debris flow impact estimation. In *Proceedings of international symposium on water management and hydraulic engineering* (ed. C. Popovska), pp. 137–148. Skopje, Macedonia: Ss Cyril and Methodius University.
- Hungr, O. (1995). A model for the runout analysis of rapid flow slides, debris flows, and avalanches. *Can. Geotech. J.* **32**, No. 4, 610–623, <https://doi.org/10.1139/t95-063>.
- Iverson, R. M. (2003). The debris-flow rheology myth. In *Debris-flow hazards mitigation: mechanics, prediction, and assessment: proceedings of the 3rd international conference on debris-flow hazards mitigation: mechanics, prediction, and assessment* (eds D. Rickenmann and C. L. Chen), pp. 303–314. Rotterdam, the Netherlands: Millpress.
- Iverson, R. M. (2015). Scaling and design of landslide and debris-flow experiments. *Geomorphology* **244**, 9–20, <https://doi.org/10.1016/j.geomorph.2015.02.033>.
- Iverson, R. M. & George, D. L. (2014). A depth-averaged debris-flow model that includes the effects of evolving dilatancy. I. Physical basis. *Proc. R. Soc. A – Math. Phys.* **470**, No. 2170, 20130819, <https://doi.org/10.1098/rspa.2013.0819>.
- Iverson, R. M., Logan, M., LaHusen, R. G. & Berti, M. (2010). The perfect debris flow? Aggregated results from 28 large-scale experiments. *J. Geophys. Res. – Earth* **115**, No. F3, article F03005, <https://doi.org/10.1029/2009JF001514>.
- Jóhannesson, T., Gauer, P., Issler, D. & Lied, K. (2009). *The design of avalanche protection dams: recent practical and theoretical developments*. Brussels, Belgium: European Commission.
- Jop, P., Forterre, Y. & Pouliquen, O. (2006). A constitutive law for dense granular flows. *Nature* **441**, No. 7094, 727–730, <https://doi.org/10.1038/nature04801>.
- Kwan, J. S. H. (2012). *Supplementary technical guidance on design of rigid debris-resisting barriers*, GEO Report No. 270. Hong Kong, China: Geotechnical Engineering Office, Civil Engineering and Development Department, Hong Kong SAR Government.
- Kwan, J. S. H. & Sun, H. W. (2006). An improved landslide mobility model. *Can. Geotech. J.* **43**, No. 5, 531–539, <https://doi.org/10.1139/t06-010>.
- Kwan, J. S. H., Koo, R. C. H. & Ng, C. W. W. (2015). Landslide mobility analysis for design of multiple debris-resisting barriers. *Can. Geotech. J.* **52**, No. 9, 1345–1359, <https://doi.org/10.1139/cgj-2014-0152>.
- Kwan, J. S. H., Sze, E. H. & Lam, C. (2019). Finite element analysis for rockfall and debris flow mitigation works. *Can. Geotech. J.* **56**, No. 9, 1225–1250, <https://doi.org/10.1139/cgj-2017-0628>.
- Li, J. G., Hamamoto, Y., Liu, Y. & Zhang, X. (2014). Sloshing impact simulation with material point method and its experimental validations. *Comput. Fluids* **103**, 86–99, <https://doi.org/10.1016/j.compfluid.2014.07.025>.
- Li, W. L., Guo, N., Yang, Z. X. & Helfer, T. (2021). Large-deformation geomechanical problems studied by a shear-transformation-zone model using the material point method. *Comput. Geotech.* **135**, 104153, <https://doi.org/10.1016/j.compgeo.2021.104153>.
- Lian, Y. P., Zhang, X. & Liu, Y. (2012). An adaptive finite element material point method and its application in extreme deformation problems. *Comput. Methods Appl. Mech. Engng* **241**, 275–285, <https://doi.org/10.1016/j.cma.2012.06.015>.
- Mast, C. M., Arduino, P., Mackenzie-Helnwein, P. & Miller, G. R. (2015). Simulating granular column collapse using the material point method. *Acta Geotech.* **10**, No. 1, 101–116, <https://doi.org/10.1007/s11440-014-0309-0>.

- McDougall, S. & Hungr, O. (2004). A model for the analysis of rapid landslide motion across three-dimensional terrain. *Can. Geotech. J.* **41**, No. 6, 1084–1097, <https://doi.org/10.1139/t04-052>.
- Monaghan, J. J. (1994). Simulating free surface flows with SPH. *J. Comput. Phys.* **110**, No. 2, 399–406, <https://doi.org/10.1006/jcph.1994.1034>.
- Morris, J. P., Fox, P. J. & Zhu, Y. (1997). Modeling low Reynolds number incompressible flows using SPH. *J. Comput. Phys.* **136**, No. 1, 214–226, <https://doi.org/10.1006/jcph.1997.5776>.
- Ng, C. W. W., Choi, C. E., Koo, R. C. H., Goodwin, G. R., Song, D. & Kwan, J. S. (2018). Dry granular flow interaction with dual-barrier systems. *Géotechnique* **68**, No. 5, 386–399, <https://doi.org/10.1680/jgeot.16.P.273>.
- Ng, C. W. W., Choi, C. E., Liu, H., Poudyal, S. & Kwan, J. S. H. (2020a). Design recommendations for single and dual debris flow barriers with and without basal clearance. In *Workshop on world landslide forum* (eds M. Sassa, S. Bobrowsky, P. T. Takara and K. Dang), pp. 33–53, [https://doi.org/10.1007/978-3-030-60196-6\\_2](https://doi.org/10.1007/978-3-030-60196-6_2). Cham, Switzerland: Springer.
- Ng, C. W. W., Wang, C., Choi, C. E., De Silva, W. A. R. K. & Poudyal, S. (2020b). Effects of barrier deformability on load reduction and energy dissipation of granular flow impact. *Comput. Geotech.* **121**, 103445, <https://doi.org/10.1016/j.compgeo.2020.103445>.
- Ng, C. W. W., Majeed, U., Choi, C. E. & De Silva, W. A. R. K. (2021). New impact equation using barrier Froude number for the design of dual rigid barriers against debris flows. *Landslides* **18**, No. 6, 2309–2321, <https://doi.org/10.1007/s10346-021-01631-7>.
- Ng, C. W. W., Majeed, U. & Choi, C. (2022). Effects of solid fraction of saturated granular flows on overflow and landing mechanisms of rigid barriers. *Géotechnique*, <https://doi.org/10.1680/jgeot.21.00170>.
- NILIM (National Institute for Land and Infrastructure Management) (2016). *Manual of technical standard for establishing Sabo master plan for debris flow and driftwood*, Technical note of NILIM no. 904. Tsukuba City, Japan: National Institute for Land and Infrastructure Management, Ministry of Land, Infrastructure and Transport.
- Pailha, M. & Pouliquen, O. (2009). A two-phase flow description of the initiation of underwater granular avalanches. *J. Fluid. Mech.* **633**, 115–135, <https://doi.org/10.1017/S0022112009007460>.
- Pouliquen, O. & Forterre, Y. (2009). A non-local rheology for dense granular flows. *Phil. Trans. R. Soc. Lond. A* **367**, No. 1909, 5091–5107, <https://doi.org/10.1098/rsta.2009.0171>.
- Randolph, M. F. & White, D. J. (2012). Interaction forces between pipelines and submarine slides – a geotechnical viewpoint. *Ocean Engng* **48**, 32–37, <https://doi.org/10.1016/j.oceaneng.2012.03.014>.
- Soga, K., Alonso, E., Yerro, A., Kumar, K. & Bandara, S. (2016). Trends in large-deformation analysis of landslide mass movements with particular emphasis on the material point method. *Géotechnique* **66**, No. 3, 248–273, <https://doi.org/10.1680/jgeot.15.LM.005>.
- Song, D., Bai, Y., Chen, X. Q., Zhou, G. G., Choi, C. E., Pasuto, A. & Peng, P. (2022). Assessment of debris flow multiple-surge load model based on the physical process of debris–barrier interaction. *Landslides* **19**, No. 2, 1165–1177, <https://doi.org/10.1007/s10346-021-01778-3>.
- Trujillo-Vela, M. G., Galindo-Torres, S. A., Zhang, X., Ramos-Cañón, A. M. & Escobar-Vargas, J. A. (2020). Smooth particle hydrodynamics and discrete element method coupling scheme for the simulation of debris flows. *Comput. Geotech.* **125**, 103669, <https://doi.org/10.1016/j.compgeo.2020.103669>.
- Van der Hoef, M. A., Beetstra, R. & Kuipers, J. A. M. (2005). Lattice-Boltzmann simulations of low-Reynolds-number flow past mono- and bidisperse arrays of spheres: results for the permeability and drag force. *J. Fluid Mech.* **528**, 233–254, <https://doi.org/10.1017/S0022112004003295>.
- VanDine, D. F. (1996). *Debris flow control structures for forest engineering*. Victoria, BC, Canada: Ministry of Forests.
- Vicari, H., Tran, Q. A., Nordal, S. & Thakur, V. (2022). MPM modelling of debris flow entrainment and interaction with an upstream flexible barrier. *Landslides* **19**, No. 9, 2101–2115, <https://doi.org/10.1007/s10346-022-01886-8>.
- Wong, H. N. (2009). Rising to the challenges of natural terrain landslides. In *Proceedings of the HKIE Geotechnical Division annual seminar on natural hillsides: study and risk management measures*, pp. 15–53. Hong Kong, China: Hong Kong Institution of Engineers.
- Zhang, F., Zhang, X., Sze, K. Y., Lian, Y. & Liu, Y. (2017). Incompressible material point method for free surface flow. *J. Comput. Phys.* **330**, 92–110, <https://doi.org/10.1016/j.jcp.2016.10.064>.
- Zhao, L., He, J. W., Yu, Z. X., Liu, Y. P., Zhou, Z. H. & Chan, S. L. (2020). Coupled numerical simulation of a flexible barrier impacted by debris flow with boulders in front. *Landslides* **17**, No. 12, 2723–2736, <https://doi.org/10.1007/s10346-020-01463-x>.